



Article

Influence of High-Pressure Torsion on the Microstructure and Microhardness of Additively Manufactured 316L Stainless Steel

Shahir Mohd Yusuf ¹, Ying Chen ² and Nong Gao ^{3,*}

- ¹ Engineering Materials and Structures (eMAST) iKohza, Malaysia-Japan International Institute of Technology (MJIT), UTM Kuala Lumpur, Universiti Teknologi Malaysia, Kuala Lumpur 54100, Malaysia; shahiryasin@utm.my
- ² Fujian Provincial Key Laboratory of Functional Materials and Applications, Xiamen University of Technology, Xiamen 361024, China; cyj829@163.com
- ³ Materials Research Group, Faculty of Engineering and Physical Sciences, University of Southampton, Southampton SO17 1BJ, UK
- * Correspondence: N.Gao@soton.ac.uk; Tel.: +44-023-8059-3396

Abstract: High-pressure torsion (HPT) is known as an effective severe plastic deformation (SPD) technique to produce bulk ultrafine-grained (UFG) metals and alloys by the application of combined compressive force and torsional shear strains on thin disk samples. In this study, the microstructures and microhardness evolution of an additively manufactured (AM) 316L stainless steel (316L SS) processed through 5 HPT revolutions are evaluated at the central disk area, where the effective shear strains are relatively low compared to the peripheral regions. Scanning electron microscopy (SEM) analysis showed that the cellular network sub-structures in AM 316L SS were destroyed after 5 HPT revolutions. Transmission electron microscopy (TEM) observations revealed non-equilibrium ultrafine grained (UFG) microstructures (average grain size: ~115 nm) after 5 revolutions. Furthermore, energy dispersive x-ray spectroscopy (EDX) analysis suggested that spherical Cr-based nano-silicates are also found in the as-received condition, which are retained even after HPT processing. Vickers microhardness (HV) measurements indicated significant increase in average hardness values from ~220 HV before HPT processing to ~560 HV after 5 revolutions. Quantitative X-ray diffraction (XRD) patterns exhibit a considerable increase in dislocation density from $\sim 0.7 \times 10^{13} \text{ m}^{-2}$ to $\sim 1.04 \times 10^{15} \text{ m}^{-2}$. The super-high average hardness increment after 5 HPT revolutions is predicted to be attributed to the UFG grain refinement, significant increase in dislocation densities and the presence of the Cr-based nano-silicates, according to the model established based on the linear additive theory.



Citation: Mohd Yusuf, S.; Chen, Y.; Gao, N. Influence of High-Pressure Torsion on the Microstructure and Microhardness of Additively Manufactured 316L Stainless Steel. *Metals* **2021**, *11*, 1553. <https://doi.org/10.3390/met11101553>

Academic Editors: Heung Nam Han and Marcello Cabibbo

Received: 6 September 2021

Accepted: 27 September 2021

Published: 29 September 2021

Publisher's Note: MDPI stays neutral with regard to jurisdictional claims in published maps and institutional affiliations.



Copyright: © 2021 by the authors. Licensee MDPI, Basel, Switzerland. This article is an open access article distributed under the terms and conditions of the Creative Commons Attribution (CC BY) license (<https://creativecommons.org/licenses/by/4.0/>).

Keywords: high-pressure torsion; laser powder bed fusion; severe plastic deformation; additive manufacturing; microstructure; microhardness

1. Introduction

High-pressure torsion (HPT) is a well-known severe plastic deformation (SPD) technique. It imposes extreme torsional strain on thin disk metallic materials that typically result in significant grain refinement down to the ultrafine regime ($<1 \mu\text{m}$), with dense dislocation networks and other nano-scale microstructural features (in some materials) [1,2]. However, the radial dependency of the torsional strain often results in heterogeneous microstructures and inhomogeneous hardness distribution across the radius of the disk [3]. Nevertheless, compared to other SPD techniques, such as equal channel angular pressing (ECAP) and accumulative roll bonding (ARB), HPT is the most efficient approach to produce significant grain refinement with large proportions of high angle grain boundaries (HAGBs) throughout the bulk material [4–6].

In particular, 316L stainless steel (316L SS) is a popular alloy that is widely used in marine, petrochemical, nuclear power, oil and gas, food and beverage, and biomedical

industries due to its exceptional resistance to corrosion, minimum rate of absorption of neutron radiation, and good ductility [7,8]. However, this alloy can not be strengthened by heat treatment procedures due to its very low carbon content, thus the only suitable means to strengthen 316L SS is by reducing the grain size, i.e., the grain refinement route (Hall–Petch mechanism) through cold working. Since only a limited grain refinement can be attained through cold working, 316L SS is a suitable alloy to be strengthened by HPT processing. In fact, numerous studies have demonstrated favourable mechanical (hardness, strength, and ductility) and functional (thermal stability, corrosion, and tribological) properties of wrought and cast 316L SS after HPT processing [9–19].

On the other hand, HPT processing has also been conducted on additively manufactured 316L SS recently by Mohd Yusuf et al. [20–23]. They have reported significant improvements in hardness, corrosion, and tribological performances after HPT processing compared to the wrought counterpart, due to the extreme grain refinement down to the nano-scale region (42 nm), nano-scale twins, combined with dense dislocation networks originating from the initial cellular sub-structures and from the HPT-induced torsional straining, and high strain rate sensitivity (SRS). Although it is known that additive manufacturing is more focused on fabricating materials with high design complexity due to the layer-wise build philosophy, another important aspect of this technology is the capability to tailor the microstructures according to the required end applications by adjusting material composition and/or processing parameters [24–26]. Therefore, as-fabricated AM metallic materials, including 316L SS often produce novel microstructures that result in mechanical and functional properties that are on par with, or even better than, the wrought/cast counterparts [27–33]. Certain post-processing techniques are also applied to improve the surface finish and integrity, such as by aging, finish machining, and blasting [34,35], as well as altering the mechanical properties of AM parts as required by post-heat treatment and/or cooling [36]. Thus, HPT processing is a viable technique to further enhance the mechanical properties of AM 316L SS [20–23].

Until now, investigations on the microstructures and mechanical properties of HPT-processed wrought/cast/AM 316L SS have always been focused on the analysis at the peripheral regions of the disk (>2.5 mm away from the centre), at which the HPT-induced torsional strain values are significantly higher than at the central area (0–2.5 mm from the centre). However, there has been almost no investigation that has been conducted at the central area that possesses low effective shear strains. In fact, the radial nature of HPT-imposed strains results in strain gradients that form geometrically necessary dislocations (GNDs), which still play an important role in influencing the changes in microstructures and mechanical properties at the central disk region [37–40]. Therefore, the main aim of this study is to investigate the evolution of microstructures and microhardness of AM 316L SS processed through 5 HPT revolutions at the central area of the disk via various microscopy techniques and Vickers microhardness (HV) measurements, respectively. Subsequently, a linear additive model is used to evaluate the respective mechanisms that contribute to the overall hardness after 5 HPT revolutions.

2. Materials and Methods

A cylindrical rod of 316L SS alloy with a length of 200 mm and diameter 10 mm was firstly additively manufactured by laser powder bed fusion (L-PBF) using a Concept Laser M2 LaserCUSING machine (Concept Laser GmbH, Lichtenfels, Germany) with the processing parameters detailed in Ref. [21]. The chemical composition of 316L SS powder and processing parameters used for L-PBF in this study are shown in Tables 1 and 2, respectively.

Table 1. Chemical composition (wt.%) of 316L SS powders used in this study.

Element	Cr	Ni	Mo	Mn	Si	P	C	S	Fe
wt.%	16.5–18.5	10.0–13.0	2.0–2.5	<2.0	<1.0	<0.045	<0.030	<0.030	Bal.

Table 2. L-PBF processing parameters used in this study.

Parameter	Value
Laser power, P (W)	200
Scan speed, v (mm s^{-1})	1600
Layer thickness (μm)	30
Scan line spacing (μm)	150
Scan strategy	Island ($5 \text{ mm} \times 5 \text{ mm}$)

To prepare the HPT samples, the rod was machined to reduce the diameter to 9.8 mm, followed by slicing into thin disks ~ 1 mm thick using wire electrical discharge machining (EDM, Able Wire EDM, Inc., Brea, CA, USA) (Figure 1a,b, respectively), and further grinding of the surface of the disks down to ~ 0.85 mm thick using 800 grits SiC paper. The disks were then subjected to 5 revolutions of HPT processing in a quasi-constrained condition under 6 GPa of pressure and speed of 1 rpm. The schematic of HPT machine setup and processing are shown in Figure 1a,b, respectively [41].

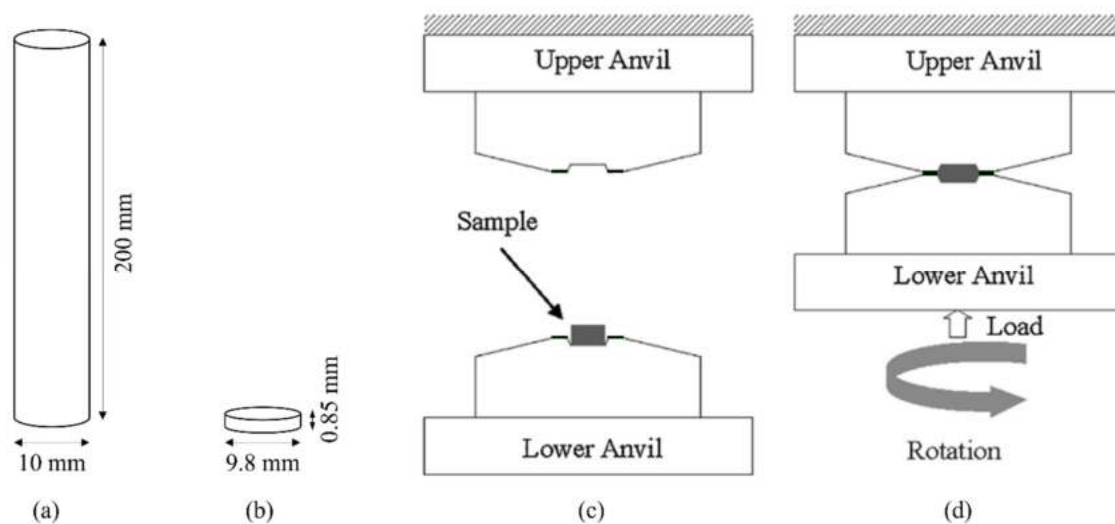


Figure 1. Size of (a) initial specimen and (b) HPT-processed samples. Schematic of HPT (c) machine setup and (d) processing. Reprinted with permission from ref. [41]. Copyright 2021 Elsevier.

After HPT-processing, the disks were further prepared for microstructural characterizations via scanning electron microscopy (SEM) through JSM JEOL 6500 FEI facility (JEOL, Tokyo, Japan), electron backscattered diffraction (EBSD, Oxford Instruments, High Wycombe, UK) through HKL Nordlys F++ camera and Aztec HKL software (Version 2.0), Oxford Instrument, High Wycombe, UK), and transmission electron microscopy (TEM) using FEI TalosTMF200S machine (mThermo Fisher Scientific, Waltham, MA, USA) equipped with energy dispersive X-ray spectroscopy, EDX (FEI, Brno-Cernovice, Czech Republic). For SEM observation, some disks were ground and polished to a mirror-like surface finish, followed by etching in Kalling's No. 2 reagent based on the procedures explained in Ref. [20]. For EBSD, some disks were electropolished in a chemical solution consisting of methanol (80%) and perchloric acid (20%) mixture at 16 V and 0.5 A for 18 s, and images were extracted within $100 \mu\text{m} \times 100 \mu\text{m}$ areas with a step size of $0.1 \mu\text{m}$ that covers > 100 grains each. SEM and EBSD images were taken at the central area of the disks, 0–2.5 mm from the centre. For TEM, some disks were mechanically ground to a thickness of $80 \mu\text{m}$ before punching smaller disks of 3 mm in diameter at the central area of the disks (0–2.5 mm from the centre). These were then dimpled using a model 656 dimple grinder and polished into thin foils using a model 695 Gatan PIPS II precision ion polishing system (Gatan Inc., Pleasanton, CA, USA). The intercept method was used to measure the average grain size from over 300 grains in 20 TEM images [42].

The phase composition before and after HPT processing was determined via X-ray diffraction (XRD) measurements using a Rigaku SmartLab X-ray Diffractometer (Rigaku, Tokyo, Japan) [21]. The peaks and peak broadening data from the XRD spectra were further analysed to evaluate the microstrain and crystallite size via Materials Analysis Using Diffraction (MAUD) software (MAUD, version 1.999, L. Lutterotti, Italy) based on the Rietveld refinement approach [43–45]. In addition, measurements for Vickers microhardness (HV) were taken along the diameter of the disk (radial direction) and throughout the disk surface in a rectilinear grid pattern using a Future Tech FM-300 microhardness tester (Future-Tech Corp, Kawasaki, Japan). The load used was 100 gf and the dwell time was 15 s, whilst the distance between each indent was set at 0.3 mm.

3. Results

3.1. Microstructural Analysis

The EBSD grain orientation map of the as-received L-PBF AM-fabricated 316L SS in Figure 2a shows overlapping melt pool squares formed due to the ‘island’ scan strategy and the angles of misorientation of the grain growth. About 19% of the grains are considered as high angle grain boundaries (HAGBs) with angles of misorientation $> 5^\circ$. These HAGBs comprised coarse and fine grains ($\sim 40\text{--}70\ \mu\text{m}$ and $\sim 10\text{--}40\ \mu\text{m}$, respectively), and very fine equiaxed grains in the range of $1\text{--}10\ \mu\text{m}$, observed at the melt pool ends/intersections. On the other hand, approximately 81% of the grains possessed misorientation angles $< 15^\circ$ and were considered as low angle grain boundaries (LAGBs). They can be observed to be contained within the interior of the HAGBs grains. Such LAGBs in AM-fabricated metals and alloys are ascribed to cellular (equiaxed or columnar) sub-structure networks that are formed due to the high cooling rate of the AM process [46]. An example of cellular sub-structure networks with numerous equiaxed cells ($\sim 1\ \mu\text{m}$) is shown in the SEM image in Figure 2b. Interestingly, Figure 2b also reveals spherical nano-sized particles between $20\text{--}100\ \text{nm}$ at the cell boundaries and within the cell interior with an average volume fraction of 0.46 vol.%. EDX point scan analysis on the spherical particles shows an average of 18.43 wt.% Cr, 14.85 wt.% Si, and 66.72 wt.% O. Thus, it can be inferred that these particles could be Cr-based nano-silicates, which is an oxide phase that are found in other studies on L-PBF AM-fabricated 316L SS as well [8,27,28,47,48].

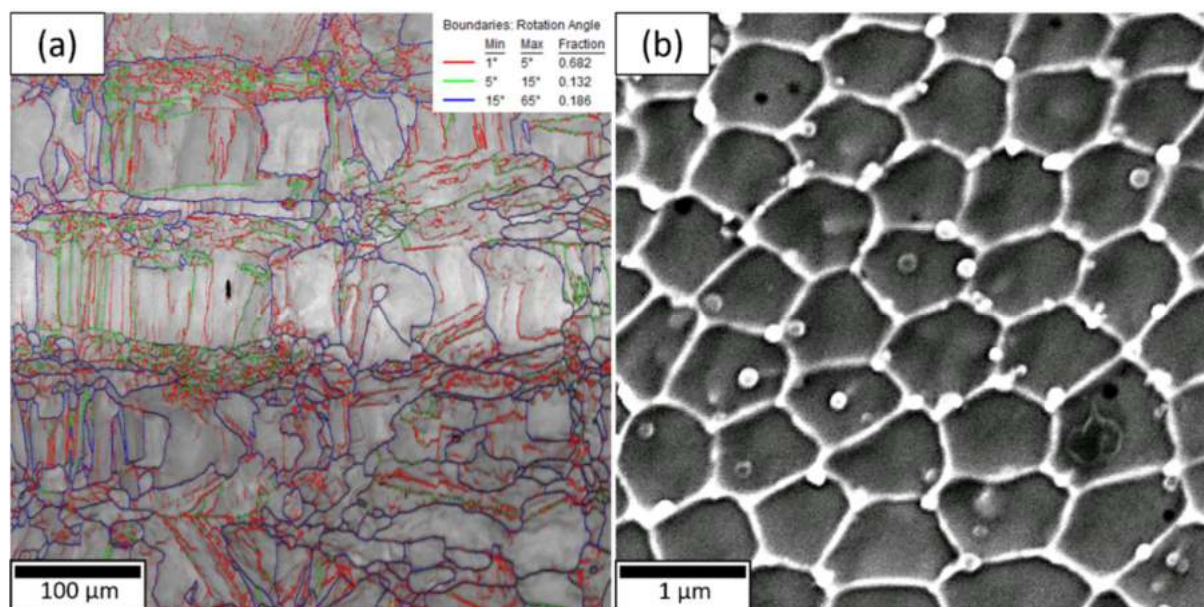


Figure 2. As-received sample: (a) Map of EBSD grain boundary misorientation and (b) SEM image showing cellular sub-structure network and random dispersions of spherical nano-sized particles.

Figure 3a shows the SEM image at the central area of the disk after 5 HPT revolutions. It is clear that the initially coherent cellular sub-structure networks are now destroyed during HPT processing. The Cr-based nano-silicate particles disappear, which implies that they are either annihilated, or possibly displaced during HPT processing. On the other hand, Figure 3b,c, respectively show the bright field (BF) and dark field (DF) TEM images of the HPT-processed disk at a similar location. These TEM images show grain refinement down to the ultrafine regime ($<1 \mu\text{m}$) with high dislocation densities and sub-grain boundaries within the grain interior (dashed red circles), which are the typical characteristics of non-equilibrium grain boundaries (GBs) obtained through SPD processing [49–51]. The average grain size is measured as $115 \pm 16 \text{ nm}$ at the central area of the disk after 5 HPT revolutions, which is in contrast with $48 \pm 11 \text{ nm}$ when measured at the disk periphery ($>3 \text{ mm}$ from its centre) based on the previous research conducted by the current authors [21].

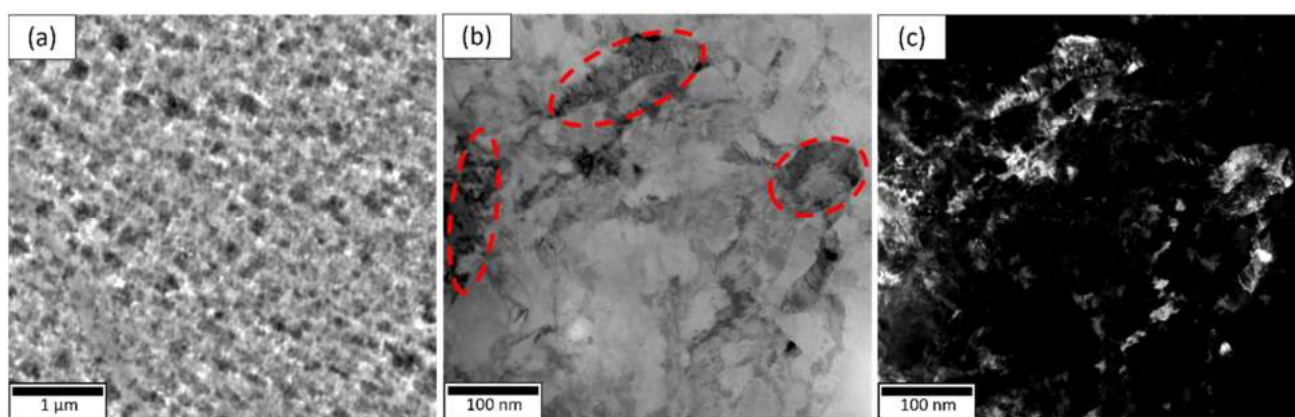


Figure 3. Central area of the disk after 5 HPT revolutions: (a) SEM image showing the annihilation of cellular sub-structure network, (b) BF-TEM image and (c) DF-TEM image revealing non-equilibrium UFG microstructures with dense dislocation densities within the grain interior.

Interestingly, further TEM observations at the central disk area reveal the presence of spherical nano-sized particles after 5 HPT revolutions, e.g., particles A and B in Figure 4a, which is suspected to be the Cr-based nano-silicates observed in the as-received disk previously. The area fraction and average diameter of the nanoparticles are determined to be 0.43% and $46 \pm 12 \text{ nm}$, respectively. EDX area scan analysis is conducted on the area shown in Figure 4a and the elemental mapping results are shown in Figure 4b–f. The EDX maps clearly indicate dispersions of Cr and O throughout the nano-sized particles, with Si being concentrated at the edges, i.e., on the outer surface of those particles. No Ni is present, while only relatively small dispersions of Fe can be observed on the particles. In addition, EDX point analysis is conducted on particles A and B to quantitatively determine the elemental compositions there, with the results shown in Table 3. The results show high wt.% of O with some Cr and Si contents, while Fe and Ni are not detected. Hence, it can be inferred that the nano-sized particles are indeed the Cr-based nano-silicates, which are not destroyed but only displaced after experiencing torsional straining through 5 HPT revolutions.

Table 3. Chemical composition (wt.%) of particles A and B in Figure 4.

Particle	Cr	Si	O	Fe	Ni
A	14.07	19.41	66.52	-	-
B	15.25	21.62	63.13	-	-

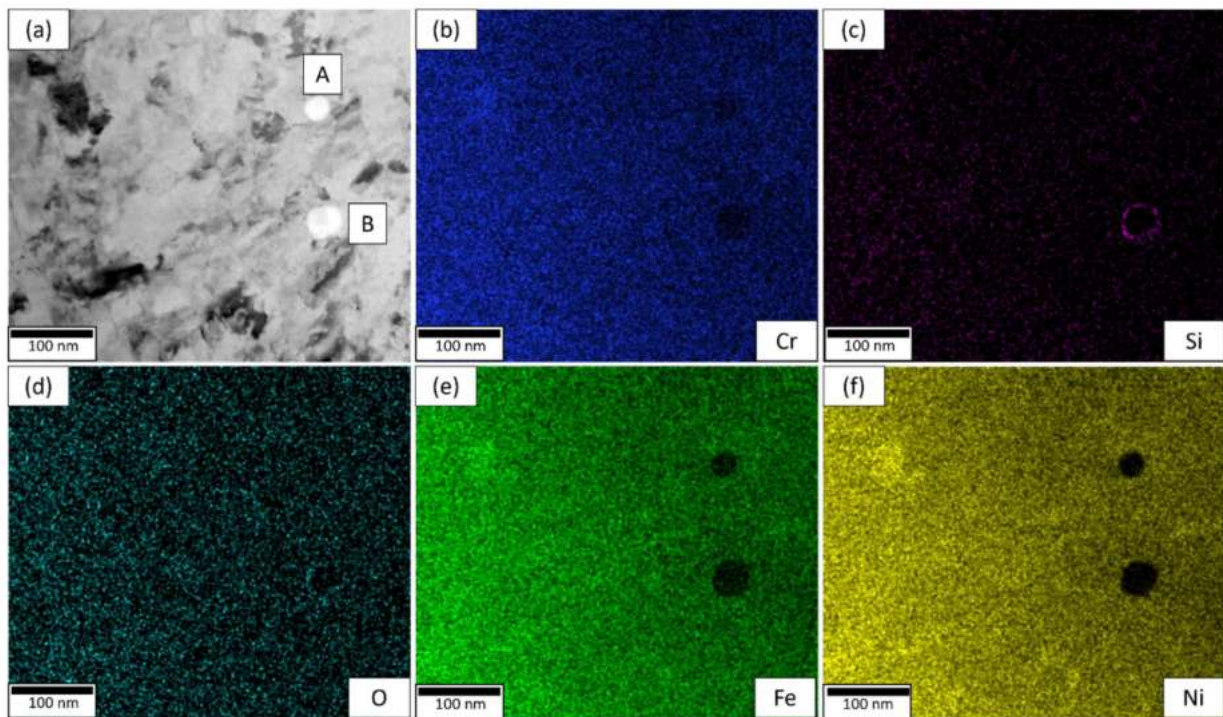


Figure 4. Central area of the disk after 5 HPT revolution: (a) BF-TEM image showing examples of spherical nano-sized particles and (b–f) corresponding EDX mapping of (a).

3.2. XRD Analysis

Figure 5 shows the XRD spectra at the central disk area for the as-received condition and after 5 HPT revolutions. The as-received sample consists of a single γ -austenite phase, although the peaks appear broadened, which is most probably due to the presence of residual stresses and dislocations induced during the fabrication process [8]. No phase change occurs and the L-PBF AM-fabricated 316L SS retains its single γ -austenitic phase even after HPT processing. However, the presence of microstrains, ε and numerous coherently scattered domains (CSD), D_c due to the torsional straining cause further broadening of the XRD peaks. The dislocation density, ρ can then be calculated by the equation as follows [52]:

$$\rho = \frac{2\sqrt{3}\langle\varepsilon^2\rangle^{1/2}}{D_c b} \quad (1)$$

where b is the Burgers vector, taken as 0.25 nm for austenitic stainless steels [53]. The Rietveld refinement method applied in MAUD software is used to obtain the values of ε and D_c through the procedures explained in Refs. [42–44]. After 5 HPT revolutions, the values of ε and D_c are estimated as $1.72 \pm 0.07 \times 10^{-3}$ and 23 ± 2 nm, respectively, while the value of ρ is calculated as $1.04 \pm 0.05 \times 10^{15} \text{ m}^{-2}$. This is a significant increase compared to $0.7 \times 10^{13} \text{ m}^{-2}$ for the as-received condition as determined by the current authors in their previous study [21].

3.3. Microhardness

Figure 6a exhibits the evolution of Vickers microhardness (HV) values along the diameter of the disk before HPT processing and after 5 HPT revolutions, in which significant hardening, ~ 2 – 3 times of the initial hardness, is attained as the result of HPT processing. However, hardness saturation, i.e., homogeneous hardness distribution throughout the disk is not achieved after 5 HPT revolutions, as illustrated by the HV mapping result shown in Figure 6b. The hardness distribution ranges from ~ 500 – 600 HV, in which the HV values increase with increasing distances towards the edge of the disk.

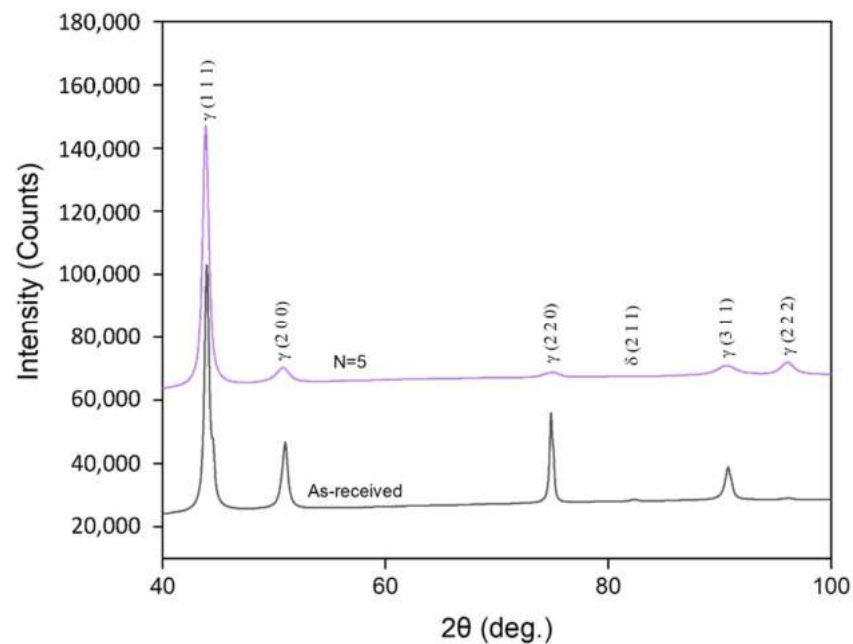


Figure 5. XRD spectra at the central area of the disk.

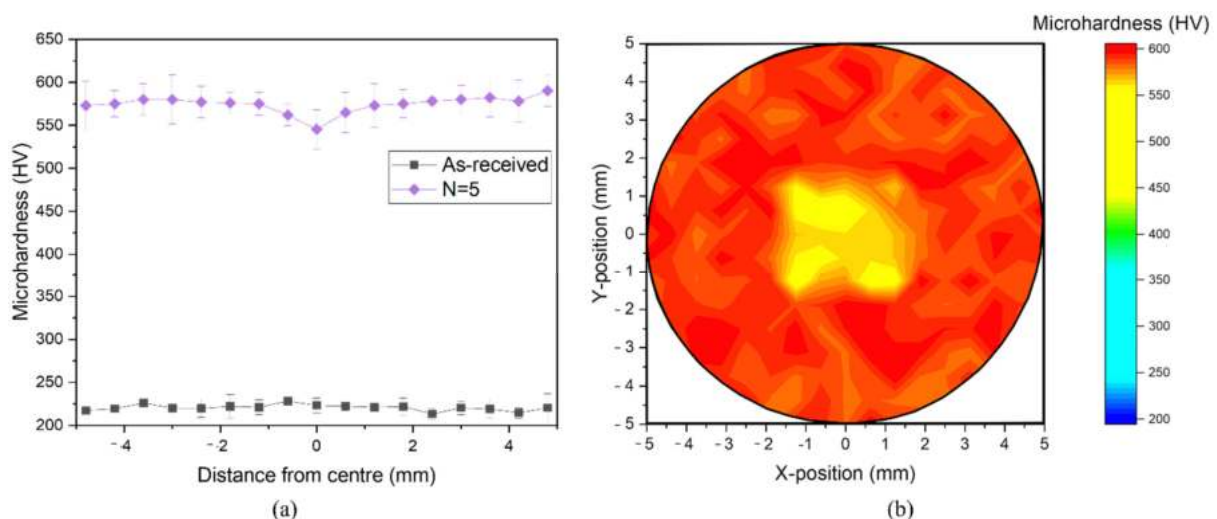


Figure 6. (a) Evolution of HV values taken along the diameter of the disk before and after 5 HPT revolutions and (b) HV mapping result throughout the HPT-processed disk after 5 revolutions.

4. Discussion

The equivalent von Mises strain, $\varepsilon_{eq.}$ in HPT-processed materials can be described as follows [4]:

$$\varepsilon_{eq.} = \frac{2\pi r N}{\sqrt{3}h} \quad (2)$$

where r is the distance from the disk centre, N is the number of HPT revolutions, and h is the disk thickness. Therefore, a radial dependency in the torsional strain values imposed throughout the disk during HPT processing is expected, in which the peripheral regions (>2.5 mm from the centre) experience higher strain hardening levels compared to the central areas (0–2.5 mm from the centre). Hence, there will be inhomogeneous distributions of grain sizes, dislocation densities, and microhardness values, particularly at low $\varepsilon_{eq.}$ values or low torsional strain levels, e.g., after 1/4, 1/2, and 1 HPT revolutions [54–59]. Such inhomogeneity is often attributed to the formation of geometrically necessary dislocations (GNDs) at the central area of the disk due to the strain gradients that are present as a result

of the radial torsional shear straining nature of the HPT process [60,61]. However, if the deformation due to HPT-imposed torsional strains exceeds certain von Mises strain values, the strain hardening level will reach a saturation stage (typically after 5 to 10 HPT revolutions), whereby the grain refinement, dislocation density generation and multiplication, and microhardness attained will be fairly homogeneous throughout the disk [3,62–67]. Moreover, there are also reports showing that such homogeneity is not achieved even after 10 HPT revolutions, which is typically attributed to the intrinsic material properties that suppresses further grain refinement or multiplication of dislocation densities, e.g., stacking fault energy (SFE) in stainless steel alloys [9,13,68,69].

In this study, although the $\varepsilon_{eq.}$ at the centre is theoretically 0 since $r = 0$, the average HV value at the central disk area is recorded as ~560 HV after HPT revolutions, which is approximately 2.5 times higher than that of the as-received condition (~220 HV). This is because in reality, strain localization takes place due to the low coefficient of strain rate sensitivity (SRS) in most HPT-processed materials, thereby some level of torsional strains are still imposed at the central area [70]. Hence, the HPT-imposed torsional straining results in severe plastic deformation that causes significant grain refinement down to the ultrafine regime (<1 μm), as well as generation and multiplication of dislocations. Indeed, Figure 3b,c show the exact consequences of such deformation; ultrafine grains with average grain size of 115 ± 16 nm with dense dislocations within the grain interior, i.e., non-equilibrium GBs are attained at the central disk area after 5 HPT revolutions. Furthermore, the analysis of the XRD spectra using MAUD software reveals that the dislocation density of $1.04 \pm 0.05 \times 10^{15} \text{ m}^{-2}$ that is significantly higher than $0.7 \times 10^{13} \text{ m}^{-2}$ before HPT processing. This confirms the SRS coefficient theory explained in Ref. [69], that torsional strains are still imposed, and dislocations are still generated and multiplied at the central disk area even though the theoretical $\varepsilon_{eq.}$ value is 0 at $r = 0$. The numerous ultrafine GBs and dense dislocation networks are known to be sites that impede dislocation motions, thereby contributing to the remarkable increase of HV values at the central disk area after 5 HPT revolutions. In addition, the spherical Cr-based nano-silicates have also been found to strengthen L-PBF AM-fabricated 316L SS by Orowan bypassing mechanism [28,48,71,72].

Therefore, a strengthening model based on the linear additive theory is used to evaluate the contribution of each mechanism to the hardness increase at the disk centre after 5 HPT revolutions. The dislocation-induced hardness increase can be estimated by the following equation [73,74]:

$$\Delta\sigma_{\rho} = CM\alpha_1Gb\sqrt{\rho_{Total}} \quad (3)$$

where C is a dimensionless constant that provides a correlation between yield strength and hardness ($C = 3$ for FCC materials [75,76]), M is the Taylor orientation factor ($M = 3.05$ for FCC materials [77]), α_1 is an empirical constant with the value 0.3 [78], G is the shear modulus, taken as 77,000 MPa for austenitic SS [77]), and ρ_{Total} is the value of dislocation density, determined as $1.04 \pm 0.05 \times 10^{15} \text{ m}^{-2}$ via XRD analysis through Equation (2). Thus, the hardness increase due to generation and multiplication of dislocations is calculated as ~174 HV. The contribution of HPT-induced grain refinement can be estimated by the Hall-Petch equation [79]:

$$\Delta\sigma_{GB} = CK_{HP}d^{-1/2} \quad (4)$$

where K_{HP} is the Hall-Petch constant that depends on the grain size regime of polycrystalline metals, taken as 0.3 MPa·m^{1/2} [77]. Meanwhile, d is the grain size, determined as 115 ± 16 nm through the line intercept method at the central disk area after 5 HPT revolutions. Therefore, the hardness increment due to the ultrafine grains is calculated as $\sim 271 \pm 8$ HV. The contribution of Cr-based nano-silicates through the Orowan mechanism can be described by [72]:

$$\Delta\sigma_{ORO} = CM\frac{Gb}{\lambda} \quad (5)$$

where λ is the average spacing of the Cr-based nano-silicates, determined as ~ 152 nm from TEM observations of 20 TEM images at the central disk area after 5 HPT revolutions. Hence, the presence of the Cr-based nano-silicates provide additional ~ 118 HV towards the overall hardness after HPT processing.

The predicted hardness based on the model used in this study is 563 ± 10 HV for the central disk area after 5 HPT revolutions, which is within the error margin and correlates well with the average hardness measured at the central disk area (0–2.5 mm from the centre) of 560 HV. Based on the estimations from this strengthening model, the highest contribution to the overall hardness is through grain boundary hardening ($\sim 48\%$), followed by dislocation hardening ($\sim 31\%$), and Orowan strengthening ($\sim 21\%$).

5. Conclusions

In this study, a 316L SS alloy was fabricated by L-PBF AM technique and then processed through 5 HPT revolutions. The microstructural evolution, phase composition and dislocation density, and hardness at the central disk area (0–2.5 mm from the centre) were assessed by microscopy technique (SEM, EBSD, and TEM), XRD analysis, and Vickers microhardness (HV) mapping approaches, respectively. A linear additive model was used to predict the contribution of different mechanisms on the overall hardness enhancement at the central disk area after 5 HPT revolutions. The following conclusions summarize the results of this study:

1. SEM, EBSD, and EDX analysis reveal that the as-received L-PBF AM-fabricated 316L SS contains unique microstructures comprising of square melt pools with LAGBs and HAGBs, cellular-sub-structure networks, and spherical Cr-based nano-silicates.
2. Microscopy observations show that the cellular sub-structure networks in the as-received disk are destroyed after 5 HPT revolutions, while the Cr-based nano-silicates are not annihilated, just displaced due to the HPT-imposed torsional strain.
3. HPT processing through 5 revolutions successfully produces ultrafine grain sizes with an average of 115 ± 16 nm, accompanied by a significant increase in dislocation density.
4. The model based on linear additive theory estimated that the hardness increase at the central disk area after 5 HPT revolutions was contributed to by grain boundary hardening ($\sim 48\%$), dislocation hardening ($\sim 31\%$) and Orowan strengthening ($\sim 21\%$).

Author Contributions: S.M.Y. contributed primarily by conducting the experiments, data collection, data analysis and writing of the manuscript; Y.C. conducted the TEM experiments and subsequent data analysis; N.G. was heavily involved in the project conceptualization, administration, and planning, as well as review and editing the manuscript. All authors have read and agreed to the published version of the manuscript.

Funding: S.M.Y. thanks the Faculty of Engineering and Physical Sciences, University of Southampton for their financial support. The TEM experiments were carried out by Y.C. with financial aids from the National Science Foundation of Fujian Province, China (No. 51601162) and High-Level Talent Funding for Xiamen Oversea Returnee.

Data Availability Statement: Data available on request due to the present investigation is part of an ongoing study.

Conflicts of Interest: The authors declare no conflict of interest.

References

1. Zhilyaev, A.; Langdon, T.G. Using high-pressure torsion for metal processing: Fundamentals and applications. *Prog. Mater. Sci.* **2008**, *53*, 893–979. [[CrossRef](#)]
2. Valiev, R.Z.; Zhilyaev, A.P.; Langdon, T.G. *Bulk Nanostructured Materials: Fundamentals and Applications*; John Wiley & Sons, Inc.: Hoboken, NJ, USA, 2014.
3. Zhilyaev, A.; Lee, S.; Nurislamova, G.; Valiev, R.; Langdon, T. Microhardness and microstructural evolution in pure nickel during high-pressure torsion. *Scr. Mater.* **2001**, *44*, 2753–2758. [[CrossRef](#)]
4. Edalati, K.; Horita, Z. A review on high-pressure torsion (HPT) from 1935 to 1988. *Mater. Sci. Eng. A* **2016**, *652*, 325–352. [[CrossRef](#)]

5. Wongsan-Ngam, J.; Kawasaki, M.; Langdon, T.G. A comparison of microstructures and mechanical properties in a Cu–Zr alloy processed using different SPD techniques. *J. Mater. Sci.* **2012**, *48*, 4653–4660. [[CrossRef](#)]
6. Valiev, R.Z.; Sabirov, I.; Zhilyaev, A.P.; Langdon, T.G. Bulk Nanostructured Metals for Innovative Applications. *JOM* **2012**, *64*, 1134–1142. [[CrossRef](#)]
7. Al-Mangour, B.; Mongrain, R.; Irissou, E.; Yue, S. Improving the strength and corrosion resistance of 316L stainless steel for biomedical applications using cold spray. *Surf. Coat. Technol.* **2013**, *216*, 297–307. [[CrossRef](#)]
8. Zhong, Y.; Liu, L.; Wikman, S.; Cui, D.; Shen, Z. Intragranular cellular segregation network structure strengthening 316L stainless steel prepared by selective laser melting. *J. Nucl. Mater.* **2016**, *470*, 170–178. [[CrossRef](#)]
9. Gubicza, J.; El-Tahawy, M.; Huang, Y.; Choi, H.; Choe, H.; Lábár, J.L.; Langdon, T.G. Microstructure, phase composition and hardness evolution in 316L stainless steel processed by high-pressure torsion. *Mater. Sci. Eng. A* **2016**, *657*, 215–223. [[CrossRef](#)]
10. El-Tahawy, M.; Huang, Y.; Choi, H.; Choe, H.; Lábár, J.L.; Langdon, T.G.; Gubicza, J. High temperature thermal stability of nanocrystalline 316L stainless steel processed by high-pressure torsion. *Mater. Sci. Eng. A* **2017**, *682*, 323–331. [[CrossRef](#)]
11. Gupta, R.; Birbilis, N. The influence of nanocrystalline structure and processing route on corrosion of stainless steel: A review. *Corros. Sci.* **2015**, *92*, 1–15. [[CrossRef](#)]
12. El-Tahawy, M.; Huang, Y.; Um, T.; Choe, H.; Lábár, J.L.; Langdon, T.G.; Gubicza, J. Stored energy in ultrafine-grained 316L stainless steel processed by high-pressure torsion. *J. Mater. Res. Technol.* **2017**, *6*, 339–347. [[CrossRef](#)]
13. El-Tahawy, M.; Gubicza, J.; Huang, Y.; Choi, H.L.; Choe, H.M.; Lábár, J.L.; Langdon, T.G. The Influence of Plastic Deformation on Lattice Defect Structure and Mechanical Properties of 316L Austenitic Stainless Steel. *Mater. Sci. Forum* **2017**, *885*, 13–18. [[CrossRef](#)]
14. El-Tahawy, M.; Pereira, P.H.; Huang, Y.; Park, H.; Choe, H.; Langdon, T.G.; Gubicza, J. Exceptionally high strength and good ductility in an ultrafine-grained 316L steel processed by severe plastic deformation and subsequent annealing. *Mater. Lett.* **2018**, *214*, 240–242. [[CrossRef](#)]
15. Hug, E.; Babu, R.P.; Monnet, I.; Etienne, A.; Moisy, F.; Pralong, V.; Enikeev, N.; Abramova, M.; Sauvage, X.; Radiguet, B. Impact of the nanostructuring on the corrosion resistance and hardness of irradiated 316 austenitic stainless steels. *Appl. Surf. Sci.* **2017**, *392*, 1026–1035. [[CrossRef](#)]
16. Kumar, B.R.; Sharma, S.; Mahato, B. Formation of ultrafine grained microstructure in the austenitic stainless steel and its impact on tensile properties. *Mater. Sci. Eng. A* **2011**, *528*, 2209–2216. [[CrossRef](#)]
17. Muley, S.; Vidvans, A.N.; Chaudhari, G.; Udainiya, S. An assessment of ultra fine grained 316L stainless steel for implant applications. *Acta Biomater.* **2016**, *30*, 408–419. [[CrossRef](#)]
18. Ralston, K.D.; Birbilis, N. Effect of Grain Size on Corrosion: A Review. *Corrosion* **2010**, *66*, 075005. [[CrossRef](#)]
19. Ralston, K.D.; Birbilis, N.; Davies, C.H.J. Revealing the relationship between grain size and corrosion rate of metals. *Scr. Mater.* **2010**, *63*, 1201–1204. [[CrossRef](#)]
20. Yusuf, S.M.; Nie, M.; Chen, Y.; Yang, S.; Gao, N. Microstructure and corrosion performance of 316L stainless steel fabricated by Selective Laser Melting and processed through high-pressure torsion. *J. Alloys Compd.* **2018**, *763*, 360–375. [[CrossRef](#)]
21. Yusuf, S.M.; Chen, Y.; Yang, S.; Gao, N. Microstructural evolution and strengthening of selective laser melted 316L stainless steel processed by high-pressure torsion. *Mater. Charact.* **2020**, *159*, 110012. [[CrossRef](#)]
22. Yusuf, S.M.; Chen, Y.; Yang, S.; Gao, N. Micromechanical Response of Additively Manufactured 316L Stainless Steel Processed by High-Pressure Torsion. *Adv. Eng. Mater.* **2020**, *22*, 2000052. [[CrossRef](#)]
23. Yusuf, S.M.; Lim, D.; Chen, Y.; Yang, S.; Gao, N. Tribological behaviour of 316L stainless steel additively manufactured by laser powder bed fusion and processed via high-pressure torsion. *J. Mater. Process. Technol.* **2021**, *290*, 116985. [[CrossRef](#)]
24. Caminero, M.Á.; Romero, A.; Chac, J.M.; Núñez, P.J.; García-plaza, E. Additive manufacturing of 316L stainless-steel structures using fused filament fabrication technology: Mechanical and geometric properties. *Rapid Prototyp. J.* **2021**, *3*, 583–591. [[CrossRef](#)]
25. Khorasani, M.; Ghasemi, A.H.; Awan, U.S.; Singamneni, S.; Littlefair, G.; Farabi, E.; Leary, M.; Gibson, I.; Veetil, J.K.; Rolfe, B. On the role of process parameters on melt pool temperature and tensile properties of stainless steel 316L produced by powder bed fusion. *J. Mater. Res. Technol.* **2021**, *12*, 2438–2452. [[CrossRef](#)]
26. Trejos, J.D.; Reyes, L.A.; Garza, C.; Zambrano, P.; Lopez-Botello, O. Numerical modeling of thermal anisotropy on a selective laser melting process. *Rapid Prototyp. J.* **2020**, *26*, 1555–1567. [[CrossRef](#)]
27. Saeidi, K.; Gao, X.; Zhong, Y.; Shen, Z. Hardened austenite steel with columnar sub-grain structure formed by laser melting. *Mater. Sci. Eng. A* **2015**, *625*, 221–229. [[CrossRef](#)]
28. Tucho, W.M.; Lysne, V.H.; Austbø, H.; Sjolyst-Kverneland, A.; Hansen, V. Investigation of effects of process parameters on microstructure and hardness of SLM manufactured SS316L. *J. Alloys Compd.* **2018**, *740*, 910–925. [[CrossRef](#)]
29. Pham, M.S.; Dovygytė, B.; Hooper, P.A. Twinning induced plasticity in austenitic stainless steel 316L made by additive manufacturing. *Mater. Sci. Eng. A* **2017**, *704*, 102–111. [[CrossRef](#)]
30. Eftefagh, A.H.; Guo, S. Electrochemical behavior of AISI316L stainless steel parts produced by laser-based powder bed fusion process and the effect of post annealing process. *Addit. Manuf.* **2018**, *22*, 153–156. [[CrossRef](#)]
31. Geenen, K.; Röttger, A.; Theisen, W. Corrosion behavior of 316L austenitic steel processed by selective laser melting, hot-isostatic pressing, and casting. *Mater. Corros.* **2017**, *68*, 764–775. [[CrossRef](#)]
32. Li, H.; Ramezani, M.; Li, M.; Ma, C.; Wang, J. Tribological performance of selective laser melted 316L stainless steel. *Tribol. Int.* **2018**, *128*, 121–129. [[CrossRef](#)]

33. Li, H.; Ramezani, M.; Li, M.; Ma, C.; Wang, J. Effect of process parameters on tribological performance of 316L stainless steel parts fabricated by selective laser melting. *Manuf. Lett.* **2018**, *16*, 36–39. [[CrossRef](#)]
34. Waqar, S.; Liu, J.; Sun, Q.; Guo, K.; Sun, J. Effect of post-heat treatment cooling on microstructure and mechanical properties of selective laser melting manufactured austenitic 316L stainless steel. *Rapid Prototyp. J.* **2020**, *26*, 1739–1749. [[CrossRef](#)]
35. Soja, A.; Li, J.; Tredinnick, S.; Woodfield, T. Surface finishing of additively manufactured stainless steel surgical instruments. *Rapid Prototyp. J.* **2021**, *1*, 59–70. [[CrossRef](#)]
36. Tascioglu, E.; Cos, M. Effect of aging and finish machining on the surface integrity of selective laser melted maraging steel. *Rapid Prototyp. J.* **2021**. [[CrossRef](#)]
37. Gao, H.; Huang, Y.; Nix, W.D.; Hutchinson, J.W. Mechanism-based strain gradient plasticity-I. Theory. *J. Mech. Phys. Solids* **1999**, *47*, 1239–1263. [[CrossRef](#)]
38. Huang, Y.; Qu, S.; Hwang, K.; Li, M.; Gao, H. A conventional theory of mechanism-based strain gradient plasticity. *Int. J. Plast.* **2004**, *20*, 753–782. [[CrossRef](#)]
39. Brinckmann, S.; Siegmund, T.; Huang, Y. A dislocation density based strain gradient model. *Int. J. Plast.* **2006**, *22*, 1784–1797. [[CrossRef](#)]
40. Mughrabi, H. On the current understanding of strain gradient plasticity. *Mater. Sci. Eng. A* **2004**, *387*, 209–213. [[CrossRef](#)]
41. Zhang, J.; Gao, N.; Starink, M.J. Al–Mg–Cu based alloys and pure Al processed by high pressure torsion: The influence of alloying additions on strengthening. *Mater. Sci. Eng. A* **2010**, *527*, 3472–3479. [[CrossRef](#)]
42. Thorvaldsen, A. The intercept method—1. Evaluation of grain shape. *Acta Mater.* **1997**, *45*, 587–594. [[CrossRef](#)]
43. Lutterotti, L.; Gialanella, S. X-ray diffraction characterization of heavily deformed metallic specimens. *Acta Mater.* **1998**, *46*, 101–110. [[CrossRef](#)]
44. McCusker, L.B.; Von Dreele, R.B.; Cox, D.E.; Louër, D.; Scardi, P. Rietveld refinement guidelines. *J. Appl. Crystallogr.* **1999**, *32*, 36–50. [[CrossRef](#)]
45. Young, R.A.; Wiles, D.B. Profile shape functions in Rietveld refinements. *J. Appl. Crystallogr.* **1982**, *15*, 430–438. [[CrossRef](#)]
46. Tucho, W.M.; Cu villier, P.; Sjolyst-Kverneland, A.; Hansen, V. Microstructure and hardness studies of Inconel 718 manufactured by selective laser melting before and after solution heat treatment. *Mater. Sci. Eng. A* **2017**, *689*, 220–232. [[CrossRef](#)]
47. Saeidi, K.; Gao, X.; Lofaj, F.; Kvetková, L.; Shen, Z.J. Transformation of austenite to duplex austenite-ferrite assembly in an-nealed stainless steel 316L consolidated by laser melting. *J. Alloys Compd.* **2015**, *633*, 463–469. [[CrossRef](#)]
48. Chen, N.; Ma, G.; Zhu, W.; Godfrey, A.; Shen, Z.; Wu, G.; Huang, X. Enhancement of an additive-manufactured austenitic stainless steel by post-manufacture heat-treatment. *Mater. Sci. Eng. A* **2019**, *759*, 65–69. [[CrossRef](#)]
49. Sauvage, X.; Enikeev, N.; Valiev, R.; Nasedkina, Y.; Murashkin, M. Atomic-scale analysis of the segregation and precipitation mechanisms in a severely deformed Al–Mg alloy. *Acta Mater.* **2014**, *72*, 125–136. [[CrossRef](#)]
50. Sauvage, X.; Wilde, G.; Divinski, S.; Horita, Z.; Valiev, R. Grain boundaries in ultrafine grained materials processed by severe plastic deformation and related phenomena. *Mater. Sci. Eng. A* **2012**, *540*, 1–12. [[CrossRef](#)]
51. Sauvage, X.; Ganeev, A.; Ivanisenko, Y.; Enikeev, N.; Murashkin, M.; Valiev, R. Grain Boundary Segregation in UFG Alloys Processed by Severe Plastic Deformation. *Adv. Eng. Mater.* **2012**, *14*, 968–974. [[CrossRef](#)]
52. Williamson, G.K.; Smallman, R.E., III. Dislocation densities in some annealed and cold-worked metals from measurements on the X-ray debye-scherrer spectrum. *Philos. Mag.* **1956**, *1*, 34–46. [[CrossRef](#)]
53. Tikhonova, M.; Enikeev, N.; Valiev, R.Z.; Belyakov, A.; Kaibyshev, R. Submicrocrystalline Austenitic Stainless Steel Processed by Cold or Warm High Pressure Torsion. *Mater. Sci. Forum* **2016**, *838*, 398–403. [[CrossRef](#)]
54. Tian, Y.Z.; Zhang, Z.F.; Langdon, T.G. Achieving homogeneity in a two-phase Cu–Ag composite during high-pressure torsion. *J. Mater. Sci.* **2012**, *48*, 4606–4612. [[CrossRef](#)]
55. Xu, C.; Horita, Z.; Langdon, T.G. The evolution of homogeneity in an aluminum alloy processed using high-pressure torsion. *Acta Mater.* **2008**, *56*, 5168–5176. [[CrossRef](#)]
56. Song, Y.; Wang, W.; Gao, D.; Yoon, E.Y.; Lee, D.J.; Lee, C.S.; Kim, H.S. Hardness and microstructure of interstitial free steels in the early stage of high-pressure torsion. *J. Mater. Sci.* **2012**, *48*, 4698–4704. [[CrossRef](#)]
57. Descartes, S.; Desrayaud, C.; Rauch, E. Inhomogeneous microstructural evolution of pure iron during high-pressure torsion. *Mater. Sci. Eng. A* **2011**, *528*, 3666–3675. [[CrossRef](#)]
58. Xu, C.; Horita, Z.; Langdon, T.G. The evolution of homogeneity in processing by high-pressure torsion. *Acta Mater.* **2006**, *55*, 203–212. [[CrossRef](#)]
59. Kawasaki, M.; Lee, H.-J.; Ahn, B.; Zhilyaev, A.; Langdon, T.G. Evolution of hardness in ultrafine-grained metals processed by high-pressure torsion. *J. Mater. Res. Technol.* **2014**, *3*, 311–318. [[CrossRef](#)]
60. Estrin, Y.; Vinogradov, A. Extreme grain refinement by severe plastic deformation: A wealth of challenging science. *Acta Mater.* **2013**, *61*, 782–817. [[CrossRef](#)]
61. Chen, Y.; Tang, Y.; Zhang, H.; Hu, N.; Gao, N.; Starink, M.J. Microstructures and Hardness Prediction of an Ultrafine-Grained Al-2024 Alloy. *Metals* **2019**, *9*, 1182. [[CrossRef](#)]
62. Loucif, A.; Figueiredo, R.B.; Baudin, T.; Brisset, F.; Langdon, T.G. Microstructural evolution in an Al-6061 alloy processed by high-pressure torsion. *Mater. Sci. Eng. A* **2010**, *527*, 4864–4869. [[CrossRef](#)]
63. Loucif, A.; Figueiredo, R.B.; Baudin, T.; Brisset, F.; Chemam, R.; Langdon, T.G. Ultrafine grains and the Hall-Petch relationship in an Al-Mg-Si alloy processed by high-pressure torsion. *Mater. Sci. Eng. A* **2012**, *532*, 139–145. [[CrossRef](#)]

64. Zhilyaev, A.; Nurislamova, G.; Kim, B.-K.; Baro, M.D.; Szpunar, J.; Langdon, T. Experimental parameters influencing grain refinement and microstructural evolution during high-pressure torsion. *Acta Mater.* **2003**, *51*, 753–765. [[CrossRef](#)]
65. Figueiredo, R.; Kawasaki, M.; Langdon, T. An Evaluation of Homogeneity and Heterogeneity in Metals Processed by High-Pressure Torsion. *Acta Phys. Pol. A* **2012**, *122*, 425–429. [[CrossRef](#)]
66. Wongsan-Ngam, J.; Kawasaki, M.; Langdon, T.G. The development of hardness homogeneity in a Cu–Zr alloy processed by equal-channel angular pressing. *Mater. Sci. Eng. A* **2012**, *556*, 526–532. [[CrossRef](#)]
67. Kawasaki, M.; Figueiredo, R.B.; Langdon, T.G. An investigation of hardness homogeneity throughout disks processed by high-pressure torsion. *Acta Mater.* **2011**, *59*, 308–316. [[CrossRef](#)]
68. Scheriau, S.; Zhang, Z.; Kleber, S.; Pippan, R. Deformation mechanisms of a modified 316L austenitic steel subjected to high pressure torsion. *Mater. Sci. Eng. A* **2011**, *528*, 2776–2786. [[CrossRef](#)]
69. Mine, Y.; Horita, Z.; Murakami, Y. Effect of hydrogen on martensite formation in austenitic stainless steels in high-pressure torsion. *Acta Mater.* **2009**, *57*, 2993–3002. [[CrossRef](#)]
70. Kulagin, R.; Beygelzimer, Y.; Ivanisenko, Y.; Mazilkin, A.; Hahn, H. Modelling of High Pressure Torsion using FEM. *Procedia Eng.* **2017**, *207*, 1445–1450. [[CrossRef](#)]
71. Hadadzadeh, A.; Baxter, C.; Amirikhiz, B.S.; Mohammadi, M. Strengthening mechanisms in direct metal laser sintered AlSi10Mg: Comparison between virgin and recycled powders. *Addit. Manuf.* **2018**, *23*, 108–120. [[CrossRef](#)]
72. Chen, B.; Moon, S.K.; Yao, X.; Bi, G.; Shen, J.; Umeda, J.; Kondoh, K. Strength and strain hardening of a selective laser melted AlSi10Mg alloy. *Scr. Mater.* **2017**, *141*, 45–49. [[CrossRef](#)]
73. Starink, M.J.; Qiao, X.G.; Zhang, J.; Gao, N. Predicting grain refinement by cold severe plastic deformation in alloys using volume averaged dislocation generation. *Acta Mater.* **2009**, *57*, 5796–5811. [[CrossRef](#)]
74. Starink, M.J.; Cheng, X.; Yang, S. Hardening of pure metals by high-pressure torsion: A physically based model employing volume-averaged defect evolutions. *Acta Mater.* **2013**, *61*, 183–192. [[CrossRef](#)]
75. Ning, J.-L.; Courtois-Manara, E.; Kurmanaeva, L.; Ganeev, A.V.; Valiev, R.Z.; Kübel, C.; Ivanisenko, Y. Tensile properties and work hardening behaviors of ultrafine grained carbon steel and pure iron processed by warm high pressure torsion. *Mater. Sci. Eng. A* **2013**, *581*, 8–15. [[CrossRef](#)]
76. Meyers, M.A.; Mishra, A.; Benson, D.J. Mechanical properties of nanocrystalline materials. *Prog. Mater. Sci.* **2006**, *51*, 427–556. [[CrossRef](#)]
77. Karavaeva, M.V.; Abramova, M.M.; Enikeev, N.A.; Raab, G.I.; Valiev, R.Z. Superior Strength of Austenitic Steel Produced by Combined Processing, including Equal-Channel Angular Pressing and Rolling. *Metals* **2016**, *6*, 310. [[CrossRef](#)]
78. Kim, J.G.; Enikeev, N.A.; Seol, J.B.; Abramova, M.M.; Karavaeva, M.V.; Valiev, R.Z.; Park, C.G.; Kim, H.S. Superior Strength and Multiple Strengthening Mechanisms in Nanocrystalline TWIP Steel. *Sci. Rep.* **2018**, *8*, 11200. [[CrossRef](#)]
79. Hansen, N. Hall–Petch relation and boundary strengthening. *Scr. Mater.* **2004**, *51*, 801–806. [[CrossRef](#)]